DISCRETE ELEMENT ANALYSIS ON ROCK WEDGE FAILURE CONSIDERING TENSILE-SHEAR COMPOSITE FAILURE OF ROCK BRIDGES

Meng-Chia Weng [1*], Tai-Tien Wang [2], Fu-Shu Jeng [2], Hoang-Khanh Le [3], Guan-Liang Lin [4]

ABSTRACT

This study investigates the mechanism of rock wedge failure by considering the tensile-shear composite failure of rock bridges through three-dimensional discrete element model (3D-DEM) simulations. The DEM model was verified using uniaxial compression, Brazilian indirect tension, and central crack Brazilian disk tests. Subsequently, the tensile strength and failure patterns of the DEM rock models with multiple existing fractures under different distributions were examined. Finally, an actual case of rock wedge failure was studied, and possible wedge failure areas were identified. According to the results, the following conclusions can be drawn: (1) The DEM model can accurately simulate laboratory tests in terms of compressive and tensile strength and their failure modes. (2) The tensile strength of the rock bridge at various rock bridge angles exhibited a U-shaped curve that was significantly affected by the rock bridge angle, spacing, and continuity. (3) The actual slope analysis shows that the tensile strength required to resist wedge failure at different rock bridge angles exhibits an inverted U-shaped curve. The upper part of the inverted U-curve was defined as a safety zone, whereas the lower part was defined as a failure zone. For low rock bridge angles ranging from −20° to 20°, rock wedge failure is prone to occur. (4) Possible wedge failure areas along an expressway were identified. Ultimately, the field investigation results agreed with the slope analysis.

Key words: Discrete element method, rock wedge failure, rock bridge, fracture propagation.

1. INTRODUCTION

Rock wedge failure, which represents rock blocks sliding down along the intersection line formed by discontinuities, is a common slope hazard of mountain roads. Rock wedge failure is a threat to the lives of road users and infrastructure safety (Varnes 1978; Hungr *et al.* 2014; Weng *et al.* 2022). For instance, numerous wedge failure events occurred along Expressway 2, a primary road along the northeastern coast of Taiwan (Fig. 1). Owing to the well-developed joints penetrating the sandstone layers, rock wedges formed easily and slid down. Sliding rock wedges usually damage expressways and disrupt transportation.

Therefore, identifying the mechanism of rock wedge failure is essential for mitigating slope disasters. Kinematic analysis is typically performed to analyze the sliding potential of a rock wedge. This method is simple, but it does not consider the failure criteria in the investigation. Considering the mechanical properties of rock masses, previous studies have evaluated the safety factor of a rock wedge system based on the limit equilibrium analysis and finite element method (FEM) (Wittke 1967; Hoek and Bray 1981; Kumsar *et al.* 2000; Xie *et al.* 2014; Moawwez *et al.* 2021; Sriyati *et al.* 2021). The aforementioned wedge failure analysis mainly

focused on assessing the shear resistance of the sliding planes and driving force. However, before the rock block slides, the fracture propagation at the top of the block is a major factor in the formation of an independent block, which is highly related to the fracture toughness of rock bridges between existing fractures. The
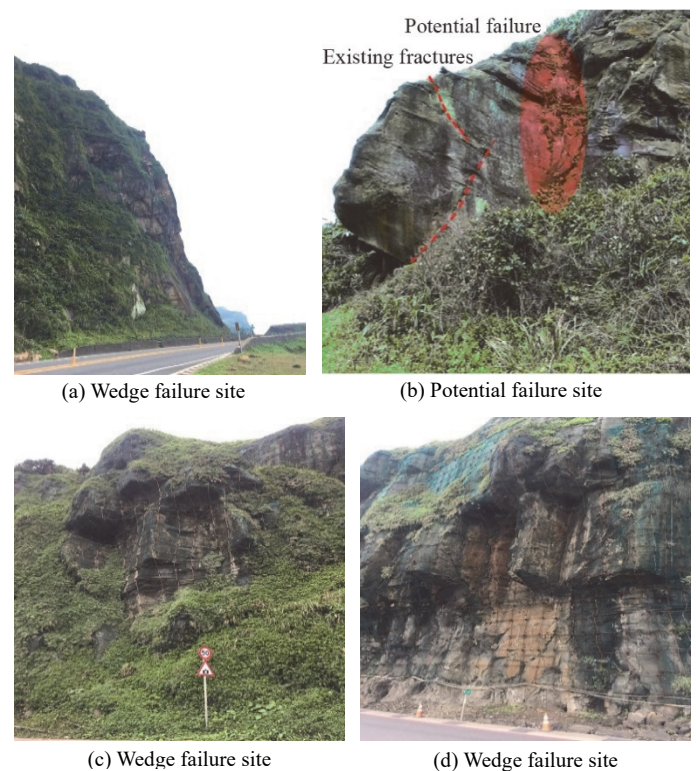

(a) Wedge failure site

(b) Potential failure site

(c) Wedge failure site

(d) Wedge failure site

Fig. 1 Rock wedge failure sites alongside 82k to 83k, Expressway 2, Taiwan

[1*] Professor (corresponding author), Department of Civil Engineering, National Yang Ming Chiao Tung University, Hsinchu, Taiwan (e-mail: mcweng@nycu.edu.tw).

[2] Professor, Department of Civil Engineering, National Taiwan University, Taipei, Taiwan.

[3] Postdoctoral researcher, Department of Civil Engineering, National Yang Ming Chiao Tung University, Hsinchu, Taiwan.

[4] Master student, Department of Civil Engineering, National Taiwan University, Taipei, Taiwan.

landslide of rock mass containing multiple joints and rock bridges commonly indicated three types of failure modes: plane failure, stepped failure, and multi-stepped failure (Eberhardt *et al.* 2004; Li *et al.* 2022). When rock bridges was broken under high tensile stresses, adjacent joint surfaces were then connected, which could form a stepped failure or multi-stepped failure. Therefore, the failure modes of bedding rock slopes, which depended on the internal and external loads, could be divided into tensile failure and tensile-shear composite failure.

Griffith (1921) developed a theoretical concept for calculating the stress value at the fracture tip of brittle materials. Irwin (1957) introduced a new term called the stress intensity factor (K) to represent the stress field at the fracture tip, which is related to the applied load, geometry of the material, and fracture. The K value increased with the applied load. The K value at the time of fracture extension and material failure is called the fracture toughness (K_c). Consequently, the fracture can be divided into three failure modes: opening, sliding, and tearing, corresponding to the fracture toughness K_I, K_{II}, and K_{III}, respectively. The fracture toughness was estimated by performing Brazilian disc tests on rock-like specimens (Lajtai 1971; Awaji and Sato 1978; Atkinson 1982; Reyes 1991; Bobet and Einstein 1998; Duan *et al.* 2015; Hu *et al.* 2017; Tiennot *et al.* 2017; Mousavi Neshad *et al.* 2018). FEM has been widely used to estimate the stress distribution around existing fractures (Johnson and Stryk 1987; Sukumar *et al.* 2000; Bouchard *et al.* 2003; Ambati *et al.* 2015; Areias *et al.* 2016). However, FEM simulation cannot reflect fracture propagation owing to the limitations of continuum theory. Compared to FEM, DEM provides more advantages in simulating the fracture mechanical behavior, even in shear or tensile modes (Lambert and Coll 2014; Weng *et al.* 2017; Borykov *et al.* 2019; Chiu and Weng 2019a; Chiu and Weng 2019b). Besides, the DEM model was wildly used to estimate the stability of rock slopes (Weng *et al.* 2020; Wu *et al.* 2021; An *et al.* 2022)

This study aims to clarify the mechanism of rock wedge failure by considering the tensile-shear composite failure of rock bridges through DEM simulations. The use of 2D simulation is faster and more simple than 3D simulation. However, we performed the 3D simulation for the investigation because the stress and geological conditions of 3D models were close to the actual model in the field. In other words, the 3D analysis could fully reflect the laboratory and prototype tests. When rock wedge failure occured, the fractures or cracks could propagate in complex directions (three-dimensional) compared to two directions in a 2D model. The 3D-DEM model was first verified by performing uniaxial compression, Brazilian indirect tension, and central crack Brazilian disk (CCBD) tests. Subsequently, the tensile strength and failure patterns of the 3D-DEM rock models with multiple existing fractures under different distributions were investigated. Finally, an actual case of rock wedge failure located at 82.5k on Expressway 2 was studied, and the possible wedge failure areas in the adjacent slopes were identified.

2. DEM ANALYSIS ON FRACTURE PROPAGATION

2.1 Laboratory Tests

In this study, a series of mechanical tests were conducted on rock-like specimens to validate the DEM analysis of fracture

propagation. The rock-like specimen was a mixture of gypsum and water at a weight ratio of 1:0.7. The unconfined compressive test (UCT) and Brazilian indirect tensile (BIT) test were performed to obtain the mechanical properties, including compressive strength, elastic modulus, Poisson's ratio, and tensile strength, of the rock-like specimens (Fig. 2). The height (H) and diameter (D) of the cylindrical UCT specimen were 130 and 54 mm, respectively, (Fig. 2(a)) with an H/D ratio of 2.41:1. The BIT test specimen was 55 mm in diameter and 27.5 mm in thickness (Fig. 2(b)). Additionally, to investigate the effect of existing fractures, we conducted a central crack Brazilian disk (CCBD) test (Fig. 2(c)). The size of the CCBD test specimen was similar to that of the BIT test specimen. A single fracture 16.5 mm long and 1 mm wide existed at the center of the CCBD specimen. The fracture formed at an angle of 45° along the vertical axis of the CCBD specimen. After casting, all specimens were cured in a moisture-controlled box (moisture = 49% and temperature = 27°C) for seven days before the test was conducted.

For the testing procedures, UCT was performed using a displacement-controlled MTS loading system with a maximum loading capacity of 4,500 kN. The specimen was loaded at a rate of 0.2 mm/min until failure. Four strain gauges (KYOWA) were used to measure the axial and radial strains. The stress, strain, and displacement test results were recorded using a data acquisition system (UCAM-60). For the BIT and CCBD tests, the loading rate was controlled at 2 mm/min using an MTS loading system with a Brazilian testing device.
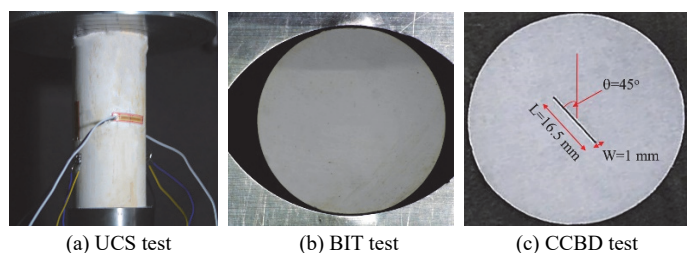

(a) UCS test   (b) BIT test   (c) CCBD test

Fig. 2   Rock-like specimens for different laboratory tests

2.2 DEM Model Setup

In this study, the DEM software (PFC3D version 5.0 by Itasca Inc. 2014) was employed to explore the mechanical behavior of rock fractures under various loading and geometric conditions. The DEM model was first validated by simulating the UCT and BIT test (Fig. 3) to obtain the micro parameters as listed in Table 1. In the UCT simulation, 27,278 ball elements, whose radius ranged from 1.5-2.0 mm, were generated in a given cylindrical space (54 mm in diameter and 130 mm in height), which was the same size as the actual UCT specimen in the laboratory (Fig. 3(a)). The parallel bond model was used as the contact model between elements (Potyondy and Cundall 2004) to simulate intergranular cementation, whose properties include normal and shear bond stiffness, normal and shear bond strength, and bond width. When the DEM model is loaded, if the resultant force between the two elements exceeds the bond strength, the parallel bond breaks, and the elements begin to slide. The force-displacement interaction between the elements follows Newton's second law of motion. The UCT and BIT test simulations were performed by moving the upper wall downward at a constant velocity of 0.2 mm/min, as performed in the test (Figs. 3(a) and 3(b)). The required model parameters for the DEM model were determined based on back analysis (Table 1).

Table 1   Microparameters used in numerical simulation

Properties	Symbol	Value	Unit
Particle density	ρ	1300	kg/m³
Young's modulus of particles	E_c	3.75	GPa
Normal/shear stiffness of particle	k_n/k_s	5.5	
Friction coefficient of particle	μ	0.5	
Parallel bond radius multiplier	λ	1.0	
Young's modulus of parallel bond	E_p	3.75	GPa
Normal/shear stiffness of parallel bond	k_{np}/k_{sp}	5.5	
Normal strength of parallel bond	σ_n	3.75	MPa
Shear strength of parallel bond	σ_s	20.0	MPa

(a) UCS model   (b) BIT model   (c) CCBD model
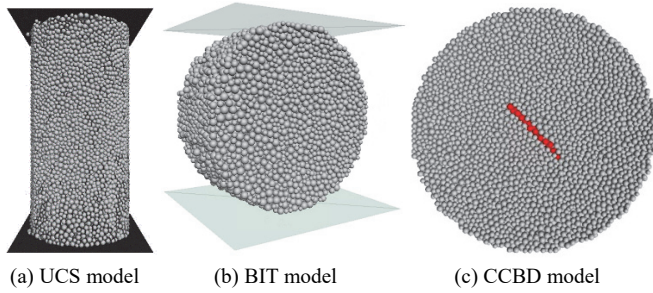
Fig. 3   DEM models for different laboratory tests

Once the DEM models of UCT and BIT test were verified with laboratory test results, the mechanical characteristics of the specimen containing a fracture (CCBD) were further investigated. The size of the CCBD model was the same as that of the BIT test model. In the CCBD model, a single fracture with a length of 16.5 mm and width of 1 mm was generated (red elements were removed in Fig. 3(c)). The contact surface among the elements inside the fracture is represented by the smooth joint model. The CCBD tests were performed at a loading rate of 2 mm/min. The failure patterns and fracture development of the DEM models during the simulation were recorded and compared with the test results.

2.3   Test Results and Model Verification

Figure 4 shows a comparison between the UCT results and numerical simulations. The simulated stress-strain curves agree well with the test results in terms of the peak strength and axial and lateral strains (Fig. 4(c)). Table 2 summarizes the mechanical properties of the test and DEM simulations. The strength of the DEM model was 10.45 MPa, which is consistent with the experimental result (10.5 MPa). The simulated elastic modulus (4.5 GPa) was also close to that of the test (4.4 GPa). A slight difference in Poisson's ratio was observed, but it did not affect the subsequent analysis. With respect to UCT failure patterns, the test and simulation results agreed well, as observed in Figs. 4(a) and 4(b).

With respect to the BIT test, the tensile strengths achieved in the experiment and simulation were 2.25 MPa and 2.23 MPa, respectively. Figure 5 shows the failure patterns of the BIT test and simulation. A centrally penetrated fracture developed in the specimen (Fig. 5(a)), and the simulation exhibited a similar failure pattern (Figs. 5(b) and 5(c)). Additionally, the simulation indicated that the BIT test specimen failed under tensile conditions. According to the abovementioned comparison, the DEM model simulated the mechanical behavior of rock-like materials reasonably and provided an accurate estimation of the strength under compressive and tensile conditions.

(a) Failure pattern of UCT   (b) Failure pattern of simulation
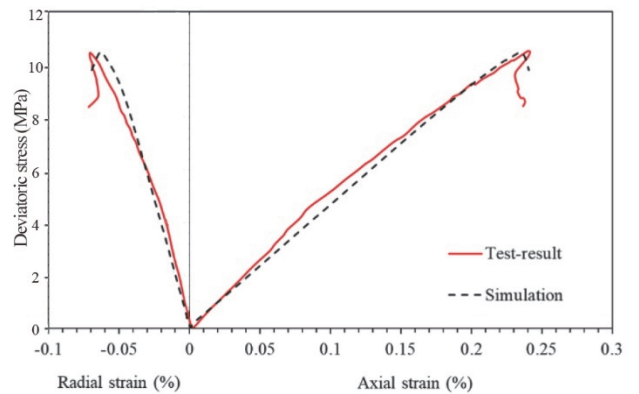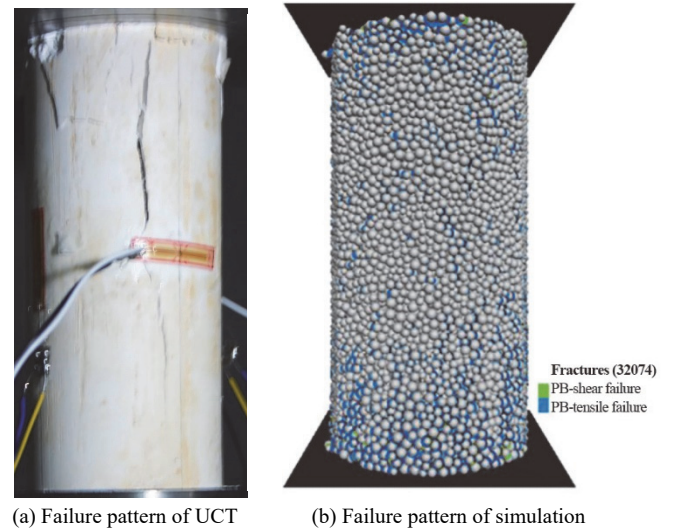
(c) Comparison on stress-strain curves between test and simulation

Fig. 4   Comparison between the UCT result and DEM simulation

Table 2   Comparison between lab test and DEM simulation

Experiment type	Properties	Test results	Simulation	Percent difference (%)
UCS test	Compressive strength (MPa)	10.5	10.45	−0.48
	Elastic modulus (GPa)	4.4	4.5	2.27
	Poisson's ratio	0.27	0.25	−7.40
BIT test	Indirect tensile strength (MPa)	2.25	2.23	0.89

(a) Failure pattern of BIT   (b) Failure pattern of simulation   (c) Development of fractures in simulation
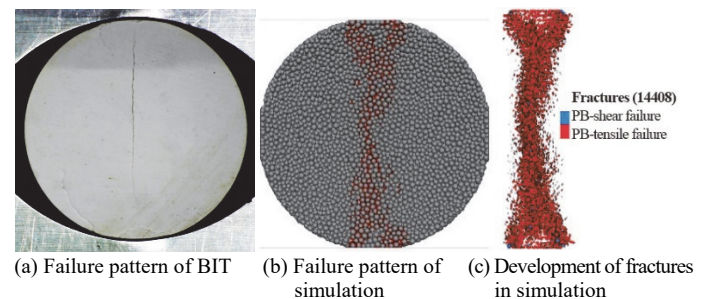
Fig. 5   Failure patterns of BIT test and DEM simulation

Figure 6 shows a comparison of the simulation and actual results of the CCBD test. In the simulation, two cracks develop from the fracture tips and propagate to the loading surface. This is consistent with the test results. The stress intensity factor at failure (fracture toughness) was evaluated using the theory proposed by Atkinson (1982).
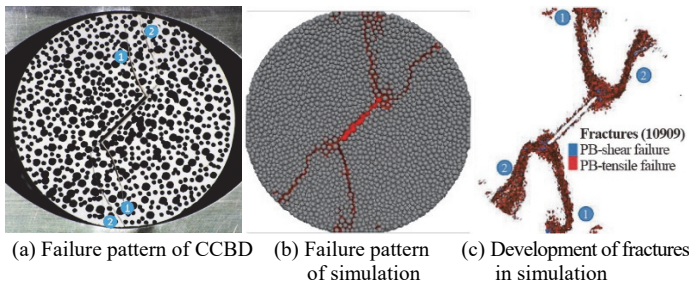
(a) Failure pattern of CCBD   (b) Failure pattern
                                    of simulation

(c) Development of fractures
    in simulation

Fig. 6   Comparison between the CCBD result and DEM simulation

$$K_I = \left[1 - 4\sin^2\theta + 4\sin^2\theta (1 - 4\cos^2\theta) \left(\frac{l}{a} \right)^2 \right] \times \frac{P}{\pi a} \sqrt{\pi l} \quad (1)$$

$$K_{II} = \sin 2\theta \left[2 + (8\cos^2\theta - 5) \left(\frac{l}{a} \right)^2 \right] \times \frac{P}{\pi a} \sqrt{\pi l} \quad (2)$$

where K_I and K_{II} are the fracture toughness in the tension and slip failure modes, respectively. θ is the angle between the fracture and loading direction, whereas P is the uniaxial load. a and l are the radius of the CCBD specimen and half length of the fracture, respectively. According to the fracture toughness results of the test and numerical simulation, K_I and K_{II} of the simulation are −9.092 kPa√m and 14.716 kPa√m, which are slightly lower than those of the laboratory test (−9.411 kPa√m and 15.233 kPa√m). The results of the CCBD simulation proved that the crack propagation and fracture toughness of rock-like materials can be accurately simulated using the DEM model.

3. ANALYSIS OF TENSILE-SHEAR COMPOSITE FAILURE OF ROCK BRIDGES

3.1 Model Setup

In this study, we further investigated the tensile-shear composite failure of rock bridges by analyzing the coalescence of two fractures under uniaxial tensile conditions. The model geometry of the double fractures, modified from Bobet and Einstein (1998), is shown in Fig. 7(a). The geometric features of the fractures included the fracture dip angle β, fracture length L, fracture spacing s, and fracture continuity c. The angle β was defined as the angle between the fracture and horizon. To explore the influence of the geometric configuration of the fractures on the tensile strength of the specimen, a series of DEM models were used. A typical cuboid DEM model with a size of 50 mm × 100 mm × 25 mm is shown in Fig. 8. The length of each fracture was 10 mm. To describe the distribution of the rock bridge between two parallel fractures, the angle of the rock bridge θ was defined as the angle between the line connecting the inner tips of the two fractures and horizon. The rock bridge angle θ measured in the clockwise direction was positive (Fig. 7(b)), whereas the angle θ in the counterclockwise direction was negative. The influence of various rock bridge angles (−75°, −60°, −45°, −30°, −20°, −10°, 0°, 10°, 20°, 30°, 45°, 60°, and 75°) on the tensile strength of the rock model was investigated. Additionally, the mechanical behavior of the rock models under different fracture spacings and continuities was evaluated. A uniaxial tensile test was simulated by stretching the two ends of the DEM model at a constant velocity of 0.02 mm/min until failure.
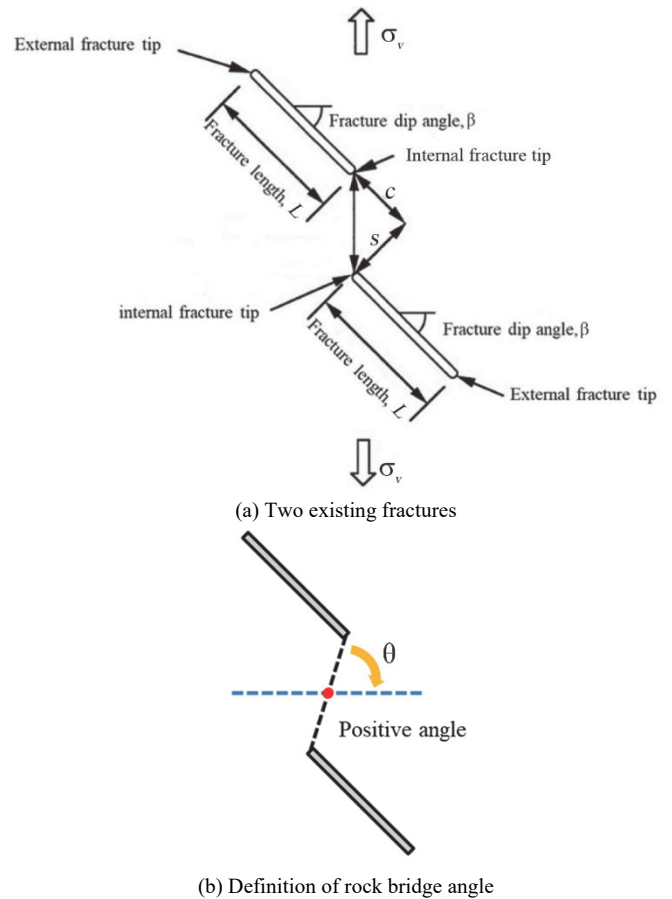

(a) Two existing fractures

(b) Definition of rock bridge angle

Fig. 7   Schematic diagram of the rock bridge between two existing fractures
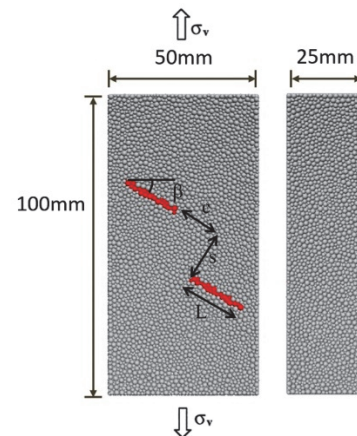

Fig. 8   DEM model with two existing fractures

3.2 Numerical Analysis Results

Figure 9, which shows the tensile strength of the rock bridge ($s = 0.50\,L$ and $c = 0.0\,L$) at various angles θ, exhibits a U-shaped curve. The results indicate that the tensile strength increased with an increase in the rock bridge angle θ for all positive angles and some negative angles (−20° to 0°). The lowest tensile strength was approximately 0.45 MPa between −10° and −30°. The models with angles of 75° and −75° showed the highest tensile strength of 0.86 MPa. Figure 10 illustrates the propagation patterns of the two

fractures inside the specimens at different rock bridge angles. The fractures developed horizontally from the external tips outside the rock bridge and extended to the surface of the specimen. The coalescence of two fractures, *i.e.,* tensile-shear composite failure, occurred only when θ ranged from −75° to 20°.
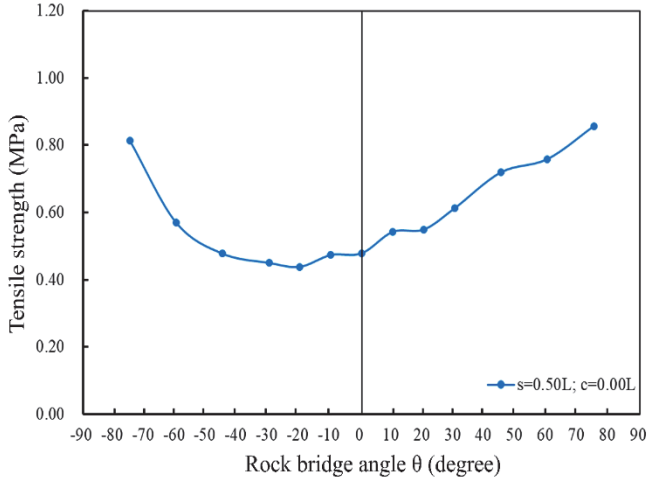
The effect of fracture spacing *s* on the tensile strength of the artificial rock models was also investigated. Considering that the fracture continuity *c* is fixed, the DEM models with fracture spacing *s* of 0.25, 0.50, 0.75, and 1.0 *L* were explored. Figure 11 shows the variations in the tensile strength at different rock bridge angles

Fig. 9   Variations of tensile strength of DEM model with two existing fractures at different rock bridge angles
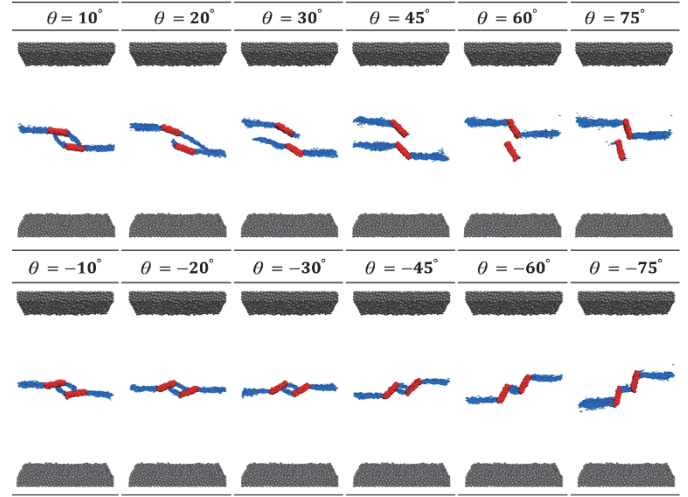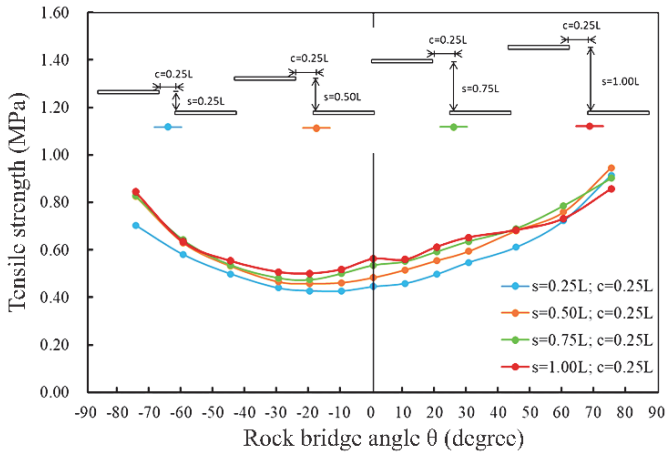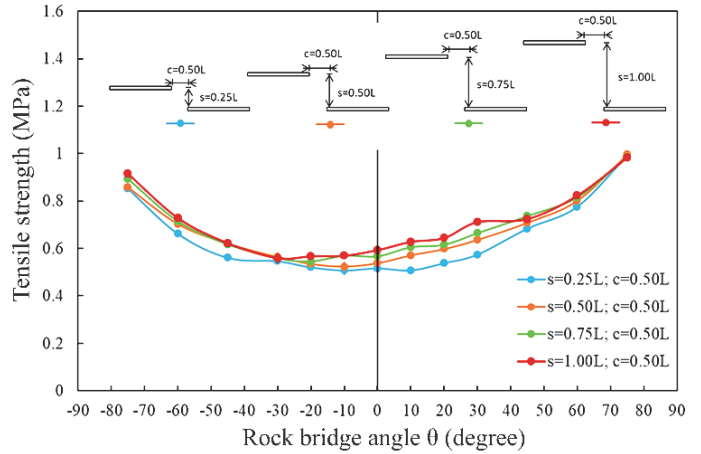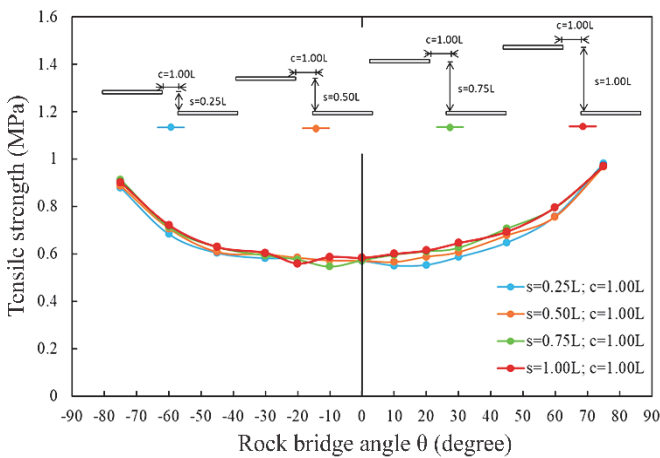

Fig. 10   Propagation patterns of two fractures inside specimens at different rock bridge angles (fracture spacing *s* = 0.5 *L* and fracture continuity *c* = 0.0 *L*)
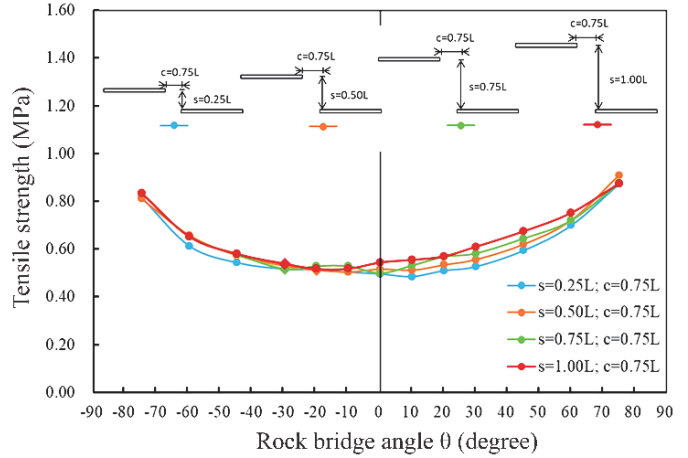

(a) Fracture continuity *c* = 0.25 *L*

(b) Fracture continuity *c* = 0.5 *L*

(c) Fracture continuity *c* = 0.75 *L*

(d) Fracture continuity *c* = 1.0 *L*

Fig. 11   Influence of fracture spacing on the tensile strength of the DEM model at different rock bridge angles

and fracture spacings. All simulated results indicate the lowest strength at an angle interval between −10° and −30°. When the fracture continuity $c = 0.25 L$ (Fig. 11(a)), the larger fracture spacing induced a higher tensile strength at rock bridge angles ranging from −80° to 60°, implying that the rock model is strongly affected by fracture spacing in this range. As the fracture continuity increased (Figs. 11(b) and 11(c)), the influence of the spacing decreased. Figure 11(d) shows that the four tensile strength curves were approximately the same. It can be concluded that the influence of the fracture spacing decreases when the fracture continuity reaches a certain distance.

Similarly, Fig. 12 shows the effect of fracture continuity on the tensile strength of rocks with existing fractures. The results indicate that the lowest tensile strength of all models occurred when the rock bridge angle ranged from 10° to −20°. For angles ranging from 20° to 75°, the tensile strength decreased with the increase in fracture continuities, whereas the opposite trend was observed from −20° to −75°. The tensile strengths of the specimens were similar at inclination angles ranging from 10° to 30°, indicating that the effect of fracture continuity was low. For negative rock bridge angles (−10° to −75°), the impact of fracture continuity was significantly reduced when the fracture spacing reached a certain value of 1.0 L. The aforementioned discussion indicates that the tensile strength and failure mechanism of the specimens were highly related to the fracture inclination angle, fracture spacing,

and fracture continuity. DEM provides a useful tool for simulating crack propagation between multiple fractures.

4. ANALYSIS ON AN ACTUAL ROCK WEDGE FAILURE

4.1 Studied Case

In this study, a discrete element analysis was conducted on an actual slope of a rock wedge failure. The studied rock slope was located at 83.6k on Expressway 2, Taiwan (Fig. 13). The geology of the studied area belongs to Miocene sedimentary rock, which mainly comprises interlayer sandstone and siltstone (Huang and Liu 1998). Rock blocks, sampled from the lower slope, were tested to determine their strength. The results of point load tests showed that the compressive strength of dry and wet sandstones were 36.60 MPa and 19.29 MPa, respectively. For siltstone, the compressive strengths under wet and dry conditions were 49.20 MPa and 14.67 MPa, respectively.

Aerial photos captured by an unmanned aerial vehicle in January 2019 were analyzed to establish a point cloud model of the rock slope. The kinematic analysis of rock slopes based on point cloud model showed that the rock wedge might slide down along the intersecting steep joint planes after coalescence of the upper fractures. Based on kinematic analysis, two joint sets were
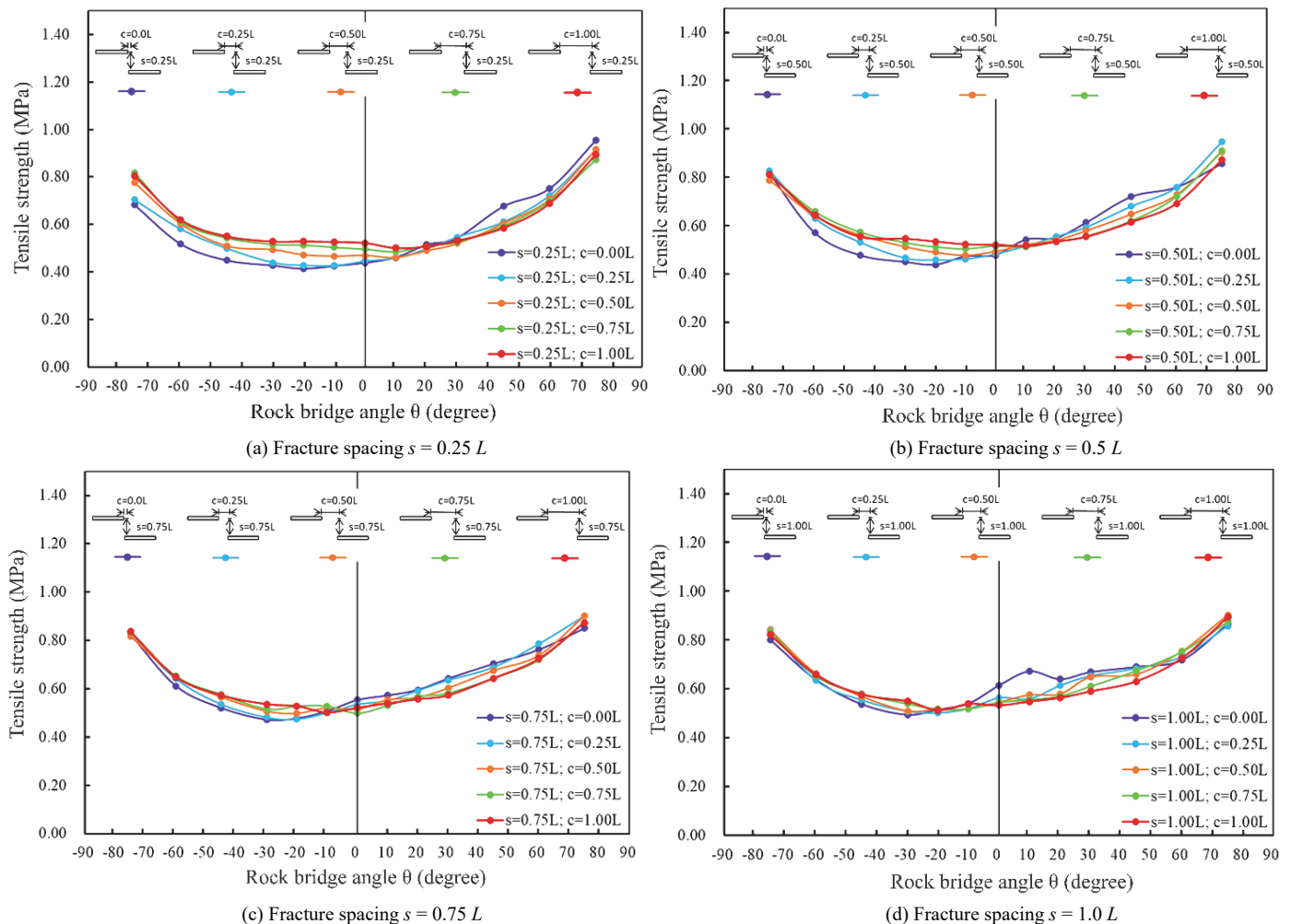

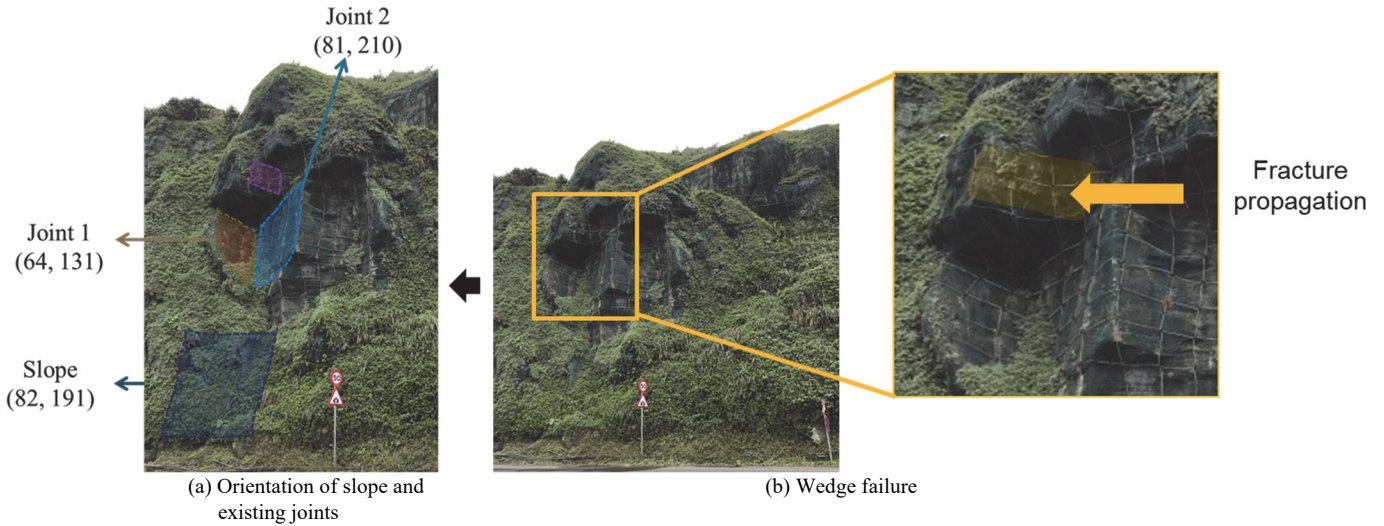**Fig. 12   Influence of fracture continuity on the tensile strength of DEM model at different rock bridge angles**

(a) Fracture spacing $s = 0.25 L$

(b) Fracture spacing $s = 0.5 L$

(c) Fracture spacing $s = 0.75 L$

(d) Fracture spacing $s = 1.0 L$

(a) Orientation of slope and existing joints

(b) Wedge failure

Fig. 13   Rock wedge failure at 83.6k on Expressway 2 in Taiwan

recognized, and the orientations of Joints 1 and 2 were (64°, 131°) and (81°, 210°), respectively, in terms of the dip angle and dip direction. The orientation of the slope surface was (82°, 191°) (Fig. 13(a)). Figure 13(b) indicates that the tensile-shear composite failure of rock bridges might occur at the top of the failure surface. This causes the rock wedge to slide down. Therefore, in this study, 3D-DEM simulations were performed to investigate the effect of fracture propagation on rock wedge stability.

4.2   DEM Model of Actual Slope

In the 3D-DEM simulation, the actual rock slope with a height of 30 m and a width of 20 m was constructed by generating 117,846 elements with an average diameter of 0.4 m (Fig. 14). The thickness of the slope top was 15 m, whereas the thickness of the slope toe was extended to 19.22 m to build a surface slope of 82°. All the elements in the DEM model were cemented using a parallel-bond model. The normal/shear stiffness of particles and parallel bonds was obtained based on back analysis, which was listed in Table 3. We performed a series of trials and errors by comparing the result of the DEM simulation and laboratory tests. Finally, the normal/shear stiffness of 5.5 showed the best fit for
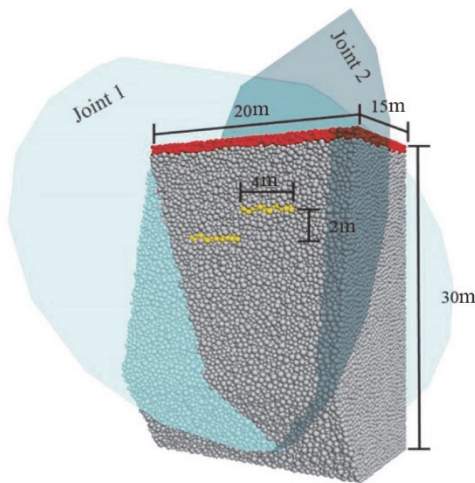
Table 3   Initial microparameters for PFC3D simulation on rock wedge failure

Properties	Symbol	Value	Unit
Young's modulus of particles	E_c	3.75	GPa
Normal/shear stiffness of particle	k_n/k_s	5.5	
Friction coefficient of particle	μ	0.5	
Young's modulus of parallel bond	E_p	3.75	GPa
Normal/shear stiffness of parallel bond	k_{np}/k_{sp}	5.5	
Normal strength of parallel bond	σ_n	3.75	MPa
Shear strength of parallel bond	σ_s	20.0	MPa

both laboratory tests and numerical simulations. For the simulation of an actual slope (Rock wedge failure at 83.6k on Expressway 2 in Taiwan), we applied the same normal/shear stiffness ratio for easier comparison and verification. Two joint sets with orientations of (64°, 131°) and (81°, 210°) were applied using the smooth joint model (light cyan planes in Fig. 14). To investigate the effect of a rock bridge on the top of a possible sliding block, two existing fractures (yellow elements) having a length of 4 m were established based on the smooth joint model. Figure 14 shows a typical model with two existing fractures with a spacing of 2 m, continuity of 0 m, and rock bridge angle of 0°. A layer of the slope top with a height of 1 m (red elements in Fig. 14) was fixed to simulate the rock block slide owing to the coalescence of the existing fractures under gravitational conditions. During the simulation, the bonding strength of the elements in the DEM model was slowly reduced until the rock wedge failure occurred. At the failure state, the fracture development and microparameters of the DEM model were recorded for analysis. Finally, BIT test with the collected microparameters was simulated to obtain the critical tensile strength of the rock model. In the following simulation, a series of models with different rock bridge angles, spacing, and continuity were considered to determine their influence on the variation in critical tensile strength.

4.3   Results and Discussion

Figure 15 shows the failure patterns of the rock bridge at various angles ranging from −75° to 90° with a fracture spacing of 0.5 L and continuity of 0.0 L. When the rock bridge angles ranged from −75° to 0°, the upper fracture developed horizontally from its

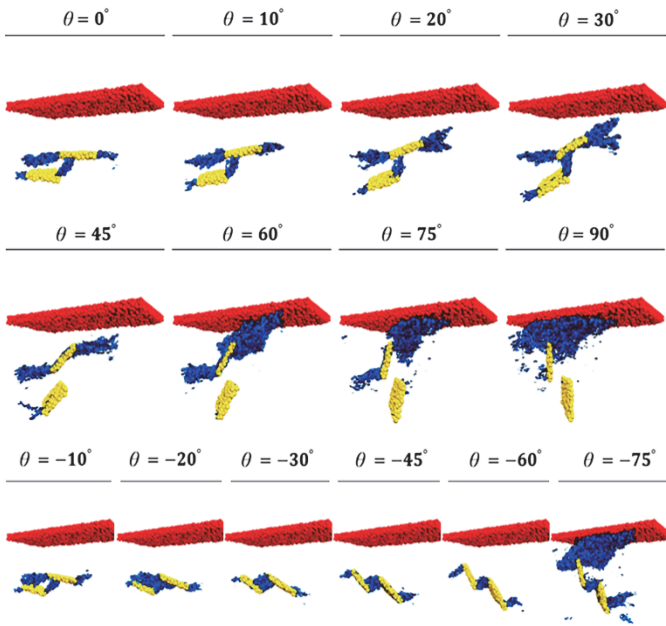**Fig. 14   DEM model for the slope regarding rock wedge failure**

Fig. 15   Fracture development of slope model at various rock bridge angles

tips and was easily connected to the lower fracture, which penetrated the entire rock block and induced the following sliding. As the rock bridge angle increased to 30°, primary failure developed along the upper fracture, and a branch of the crack grew from the lower fracture to the upper fracture. However, as the rock bridge angles ranged from 45° to 90°, the primary failure developed only from the upper fracture and did not propagate to the lower fracture. Furthermore, the tensile strengths of all DEM models can be calculated from BIT tests. Figure 16 shows the variations in the tensile strength required to resist wedge failure at different rock bridge angles. Inverted U-shaped curves ranging from −60° to 60° were observed. Rock wedge failure occurs when the tensile strength of the rock is lower than that of the curve. This indicates that the tensile stress is larger than the tensile strength of the rock. Therefore, in this study, the upper part of the inverted U-curve was defined as a safety zone, whereas the lower part was defined as a failure zone. The peak values of the required tensile strength are located at low angles ranging from −20° to 20°, indicating that rock wedge failure was prone to occur. As the fracture continuity increases from 0.0 L to 0.50 L, the peak values of the required tensile strength shifted from the left (negative angles) to the right (positive angles), resulting in a larger safety zone. When the angle was lower than 20°, the safety zone increased with fracture continuity. However, the safety zone decreases with an increase in the fracture continuity if the angle is higher than 20°. All tensile strength curves were the same at angles higher than 60° and lower than −60°, indicating that the slope was relatively stable and was not affected by the change in fracture continuity.

The results of Fig. 16 can be further applied to identify the possible wedge failure area in the adjacent slopes along Expressway 2. Figures 17(a) and 17(b) shows that the study area is located at the limb of a syncline, and the dip angle of the rock layer varies with distance from the fold axis. The dip angles of the rock layers were measured using the point cloud model, and the results showed that the dip angles, ranging from 5.3° to 15.7°, increased

from the east (left side) to the west (right side) (Figs. 17(c) and 17(d)). According to Fig. 16, if the dip angle of the rock layer becomes gentler (less than 20°), wedge failure is likely to occur. The entire rock layer exhibited the potential for wedge failure. However, the rock layer with a lower dip angle (Fig. 17(c)) indicated a higher potential for rock wedge failure. The field investigation also agreed with the numerical analysis, *i.e.,* wedge failure occurred frequently on slopes with a nearly horizontal rock layer.
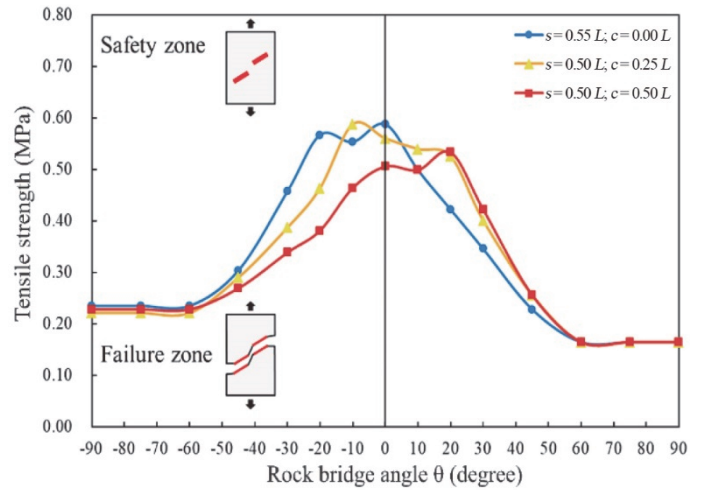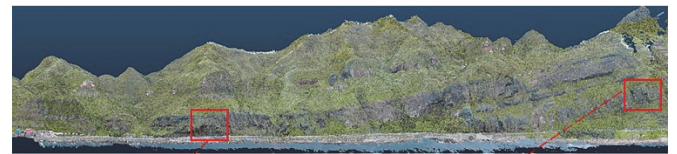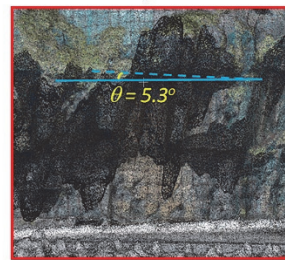

Fig. 16   Variation of required tensile strength to resist wedge failure at different rock bridge angles

(a) Plan view of the study area

(b) Front view of the study area

(c) Rock layer with a lower dip angle   (d) Rock layer with a higher dip angle

Fig. 17   Possible wedge failure area in the adjacent slopes along Expressway 2

5.   CONCLUSIONS

In this study, we investigated the mechanism of rock wedge failure by considering the tensile-shear composite failure of rock bridges using 3D-DEM simulations. The DEM model was first verified by uniaxial compression, BIT, and CCBD tests. Subsequently, the tensile strength and failure patterns of the DEM rock models with multiple existing fractures under different distributions were examined. Finally, an actual case of rock wedge failure, located at 82.5k on Expressway 2, was studied, and the possible wedge failure areas in the adjacent slopes were identified. Based on the results, the following conclusions can be drawn.

1. The simulation results of uniaxial compression, BIT, and CCBD tests prove that the DEM model can simulate the crack propagation and fracture toughness of rock-like materials accurately.

2. With respect to the tensile-shear composite failure of rock bridges between two existing fractures, the results indicate that the tensile strength of the rock bridge at various rock bridge angles exhibits a U-shaped curve. The lowest tensile strength was observed at angles ranging from $-10°$ to $-30°$. The models with $75°$ and $-75°$ angles showed the highest tensile strength. The tensile strength decreased with increasing fracture spacing and fracture continuity. Additionally, DEM provides a useful tool for simulating crack propagation between multiple fractures.

3. In the rock wedge failure analysis of the slope, the tensile strength required to resist wedge failure at different rock bridge angles was obtained. A series of inverted U-shaped curves were observed. Rock wedge failure occurs when the tensile strength of the rock is lower than that of the curves. This indicates that the tensile stress is larger than the tensile strength of the rock. Accordingly, we defined the upper part of the inverted U curves as a safety zone and the lower part as a failure zone for further engineering practice.

4. Possible wedge failure areas in the adjacent slopes along Expressway 2 were identified. A rock layer with a lower dip angle indicates a higher potential for a rock wedge failure. Furthermore, the field investigation agreed with the numerical analysis, *i.e.,* wedge failure occurred frequently on slopes with a nearly horizontal rock layer.

FUNDING

DATA AVAILABILITY

The data and/or computer codes used/generated in this study are available from the corresponding author on reasonable request.

CONFLICT OF INTEREST STATEMENT

The authors declare that there is no conflict of interest.

REFERENCES

Ambati, M., Gerasimov, T., and De Lorenzis, L. (2015). "Phase-field modeling of ductile fracture." *Computational Mechanics*, **55**(5), 1017-1040. https://doi.org/10.1007/s00466-015-1151-4

An, Y., Yan, Y.C., Li, L., Li, X.M., and Huang, S.P. (2022). "Stability analysis method of scattered-shape unstable rock mass." *Journal of GeoEngineering*, **17**(1), 011-021. http://dx.doi.org/10.6310/jog.202203_17(1).2

Areias, P., Rabczuk, T., and Msekh, M.A. (2016). "Phase-field analysis of finitestrain plates and shells including element subdivision." *Computer Methods in Applied Mechanics and Engineering*, **312**, 322-350. https://doi.org/10.1016/j.cma.2016.01.020

Atkinson, C., Smelser, R.E., and Sanshez, J. (1982). "Combined mode fracture via the cracked Brazilian disk test." *International Journal of Fracture*, **18**(4), 279-291. https://doi.org/10.1007/BF00015688

Awaji, H. and Sato, S. (1978). "Combined mode fracture toughness measurement by the disk test." *Journal of Engineering Materials and Technology*, **100**, 175-182. https://doi.org/10.1115/1.3443468

Bobet, A. and Einstein, H.H. (1998). "Fracture coalescence in rock-type materials under uniaxial and biaxial compression." *International Journal of Rock Mechanics and Mining Sciences*, **35**(7), 863-888. https://doi.org/10.1016/S0148-9062(98)00005-9

Bouchard, P.O., Bay, F., and Chastel, Y. (2003). "Numerical modelling of crack propagation: automatic remeshing and comparison of different criteria." *Computer Methods in Applied Mechanics and Engineering*, **192**(35), 3887-3908. https://doi.org/10.1016/S0045-7825(03)00391-8

Chiu, C.C. and Weng, M.C. (2019a). "DEM simulation of planar sliding using a particulate interface model considering velocity-dependent friction." *Computers and Geotechnics*, **112**, 51-59. https://doi.org/10.1016/j.compgeo.2019.04.001

Chiu, C.C. and Weng, M.C. (2019b). "Simulating interface characteristics by using a particulate interface model of a discrete element method." *Computers and Geotechnics*, **109**, 1-11. https://doi.org/10.1016/j.compgeo. 2019.01.011

Duan, K. and Kwok, C.Y. (2015). "Discrete element modeling of anisotropic rock under Brazilian test conditions." *International Journal of Rock Mechanics and Mining Sciences*, **78**, 46-56. https://doi.org/10.1016/j.ijrmms.2015.04.023

Eberhardt, E., Stead, D., and Coggan, J.S. (2004). "Numerical analysis of initiation and progressive failure in natural rock slopes - the 1991 Randa rockslide." *International Journal of Rock Mechanics and Mining Sciences*, **41**(1), 69-87. https://doi.org/10.1016/S1365-1609(03)00076-5

Griffith, A.A. (1921). "The phenomena of rupture and flow in solid." *Philosophical Transactions of the Royal Society of London*, **221**, 163-198. https://doi.org/10.1098/rsta.1921.0006

Hoek, E. and Bray, J.W. (1981). *Rock Slope Engineering*, 3rd Ed., Institute of Mining and Metallurgy, London, 358. https://doi.org/10.1201/9781482267099

Hu, S.C., Tan, Y.I., Zhou, H., Guo, W.Y., Hu, D.W., Meng, F.Z., and Liu, Z.G. (2017). "Impact of bedding planes on mechanical properties of sandstone." *Rock Mechanics and Rock Engineering*, **50**, 2243-2251. https://doi.org/10.1007/s00603-017-1239-6

Huang, C.S. and Liu, H.C. (1988). *Geological Map of Taiwan Scale 1:50,000;05*. Central Geological Survey, Taiwan.

Hungr, O., Leroueil, S., and Picarelli, L. (2014). "The Varnes classification of landslide types, an update." *Landslides*, **11**, 167-194. https://doi.org/10.1007/s10346-013-0436-y

Irwin, G. (1957). "Analysis of stresses and strains near the end of a crack traversing a plate." *Journal of Applied Mechanics*, **24**, 361-364. https://doi.org/10.1115/1.4011547

Itasca Consulting Group, Inc. (2014). *PFC – Particle Flow Code*, Ver. 5.0. Minneapolis, MN: Itasca.

Johnson, G.R. and Stryk, R.A. (1987). "Eroding interface and improved tetrahedral element algorithms for high-velocity impact computations inthree dimensions." *International Journal of Impact Engineering*, **5**(1), 411-421. https://doi.org/10.1016/0734-743X(87)90057-1

Kumsar, H., Aydan, O., and Ulusay, R. (2000). "Dynamic and static stability assessment of rock slopes against wedge failures." *Rock Mechanics and Rock Engineering*, **33**(1), 31-51. https://doi.org/10.1007/s006030050003

Lajtai, E.Z. (1971). "A theoretical and experimental evaluation of the Griffith theory of brittle fracture." *Tectonophysics*, 11, 129-156. https://doi.org/10.1016/0040-1951(71)90060-6

Lambert, C. and Coll, C. (2014). "Discrete modeling of rock joints with a smooth-joint contact model." *Journal of Rock Mechanics and Geotechnical Engineering*, **6**, 1-12. https://doi.org/10.1016/j.jrmge.2013.12.003

Li, D.J., Jia, W.T., Cheng, X., Zhao, L.H., Zhang, Y.B., and Yu, P.C. (2022). "Limit state analysis of stepped sliding of jointed rock slope based on tensile-shear composite failure mode of rock bridges." *Bulletin of Engineering Geology and The Environment*, **81**(6), 233. https://doi.org/10.1007/s10064-022-02731-x

Moawwez, M.A., Wang, J., and Hussain, M. A. (2021). "Development of empirical correlations for limit equilibrium methods of slope stability analysis." *Arabian Journal of Geosciences*, **14**. https://doi.org/10.1007/s12517-021-08375-7

Mousavi N.M., Fisher, Q.J., Gironacci, E., and Rezania, M. (2018). "Experimental study and numerical modeling of fracture propagation in shale rocks during brazilian disk test." *Rock Mechanics and Rock Engineering*, **51**, 1755-1775. https://doi.org/10.1007/s00603-018-1429-x

Potyondy, D.O. and Cundall, P.A. (2004). "A bonded-particle model for rock." *International Journal of Rock Mechanics and Mining Sciences*, **41**(8), 1329-1364. https://doi.org/10.1016/j.ijrmms.2004.09.011

Reyes, O.M. (1991). *Experimental Study and Analytical Modelling of Compressive Fracture in Brittle Materials*. Ph.D. Dissertation, Department of Civil Engineering, Massachusetts Institute of Technology: Boston.

Sriyati, R., Martini, M., Mastura, L., Shafira, Y. A. (2021). "Investigation of potential landslides due to liquefaction on the balaroa road section using the limit equilibrium method." *Journal of Applied Engineering Science*, **19**(3), 556-563. https://orcid.org/0000-0002-6614-0984

Sukumar, N., Moes, N., Moran, B., and Belytschko, T. (2000). "Extended finite element method for three-dimensional crack modelling." *International Journal for Numerical Methods in Engineering*, **48**(11), 1549-1570. https://doi.org/10.1002/1097-0207(20000820)48:11<1549::AID-NME955>3.0.CO;2-A

Tiennot, M., Mertz, J.D., and Bourges, A. (2017). "Influence of anisotropic microcracking due to swelling on the fracture toughness of a claybearing sandstone." *Rock Mechanics and Rock Engineering*, **50**, 2861-2870. https://doi.org/10.1007/s00603-017-1273-4

Varnes, D.J. (1978). *Slope Movement Types and Processes*. Special report, **176**, 11-33.

Weng, M.C., Chen, T.C., and Tsai, S.J. (2017). "Modeling scale effects on consequent slope deformation by centrifuge model tests and the discrete element method." *Landslides*, **14**, 981-993. https://doi.org/10.1007/s10346-016-0774-7

Weng, M.C., Jeng, F.S., Chiu, C.C., and Lin, Y.C. (2020). "Modeling rock bolt reinforcement by using the particulate interface model of DEM." *Journal of GeoEngineering*, **15**(3), 123-134. https://doi.org/10.6310/jog.202009_15(3).2

Weng, M.C., Lin, C.H., Shiu, W.J., Chao, W.A., Chiu, C.C., Lee, C.F., Huang, W.K., and Yang, C.M. (2022). "Toward a rapid assessment of highway slope disasters by using multidisciplinary techniques." *Landslides*, **19**, 687-701. https://doi.org/10.1007/s10346-021-01808-0

Wittke, W. (1967). "Infuence of the shear strength of joints on the design of prestressed anchors to stabilize a rock slope." *Geotechnical Conference*, Oslo, Paper No. 4.11, 311-318.

Wu, J.H. and Hsieh, P.H. (2021). "Numerical assessment of the impact area and the geometry of a landslide dam: the Nan-Shi-Keng landslide, Taiwan." *Journal of GeoEngineering*, **16**(4), 155-167. http://dx.doi.org/10.6310/jog.202112_16(4).4

Xie, X., Liu, Y., Han, J., and Xing, L. (2014). "3D finite element numerical analysis for stability calculation of high steep rock slope." *Advances in Civil and Industrial Engineering*, 580-583, 532-538. https://doi.org/10.4028/www.scientific.net/AMM.580-583.532